LAWRENCE
LIVERMORE
NATIONAL
LABORATORY

LLNL-JRNL-643193

First measurement of Am-240(n,f) surrogate cross section

R. J. Casperson, J. T. Burke, N. D. Scielzo, J. E. Escher, M. McCleskey, A. Saastamoinen, E. Simmons, A. Spiridon, A. Ratkiewicz, A. Blanc, M. Kurokawa, R. G. Pizzone

August 30, 2013

Physical Review C

Disclaimer

This document was prepared as an account of work sponsored by an agency of the United States government. Neither the United States government nor Lawrence Livermore National Security, LLC, nor any of their employees makes any warranty, expressed or implied, or assumes any legal liability or responsibility for the accuracy, completeness, or usefulness of any information, apparatus, product, or process disclosed, or represents that its use would not infringe privately owned rights. Reference herein to any specific commercial product, process, or service by trade name, trademark, manufacturer, or otherwise does not necessarily constitute or imply its endorsement, recommendation, or favoring by the United States government or Lawrence Livermore National Security, LLC. The views and opinions of authors expressed herein do not necessarily state or reflect those of the United States government or Lawrence Livermore National Security, LLC, and shall not be used for advertising or product endorsement purposes.

Measurement of the ^{240}Am(n,f) cross section using the surrogate ratio method

R. J. Casperson,* J. T. Burke, N. D. Scielzo, and J. E. Escher
Lawrence Livermore National Laboratory, Livermore, California 94551

M. McCleskey, A. Saastamoinen, E. Simmons, and A. Spiridon
Cyclotron Institute, Texas A&M University, College Station, Texas 77843

A. Ratkiewicz
Department of Physics and Astronomy, Rutgers University, New Brunswick, New Jersey 08903

A. Blanc
Institut Laue-Langevin, B.P. 156, F-38042 Grenoble Cedex 9, France

M. Kurokawa
RIKEN Nishina Center, Wako, Saitama 351-0198, Japan

R. G. Pizzone
Istituto Nazionale di Fisica Nucleare - Laboratori Nazionali del Sud, I-95123 Catania, Italy
(Dated: June 24, 2014)

The ^{240}Am(n,f) cross section has been measured for the first time above 4 MeV, using the surrogate ratio method over the neutron energy range of 200 keV to 14 MeV. The reactions ^{243}Am(p,tf) and ^{238}U(p,tf), which proceed through the fissioning excited nuclei ^{241}Am* and ^{236}U*, were used as surrogates for the desired ^{240}Am(n,f) and ^{235}U(n,f) reactions. The experiment was fielded using the STARLiTeR detector system with a recently commisioned VME-based data acquisition system. The 38.4 MeV proton beam used in these measurements was provided by the K150 cyclotron at the Texas A&M Cyclotron Institute. The measured ^{240}Am(n,f) cross section disagrees with many of the most recent evaluations, and a reevaluation is recommended.

PACS numbers: 25.40.Hs, 24.75.+i, 24.87.+y, 25.85.Ec

I. INTRODUCTION

The surrogate ratio method is a useful technique for determining reaction cross sections on short-lived targets, which would otherwise be unmeasurable. Originally used by Cramer and Britt in 1970 [1, 2], it has found recent use in the determination of several neutron-induced fission cross sections over the past decade [3–16]. The method builds on the assumption that the decay of the compound nucleus is independent of its formation. In a surrogate experiment, the compound nucleus of interest is produced by using a direct reaction with a more accessible projectile-target combination, and observables indicating the decay of the compound nucleus are measured in coincidence with the ejectile from the direct reaction. The measurements are then combined with a theoretical treatment of the process to extract the neutron-induced cross section from the measured data. Theoretical input may include, depending on the case under consideration, the calculation of the compound-formation cross section, the prediction of spin-party distributions resulting from the direct reaction, and Hauser-Feshbach-type modeling of the compound-nuclear decay [15].

For fission applications, it is typically sufficient to employ the Weisskopf-Ewing approximation, which ignores the difference in the spin-parity distribution between the neutron-induced and direct reactions [17, 18]. This approximation eliminates the need for theoretical descriptions of the direct reaction and modeling of the compound decay.

The surrogate ratio approach is a variant of the surrogate method that assumes the approximate validity of the Weisskopf-Ewing limit and has various experimental advantages. For the reactions being considered in this work, the ratio

$$\mathrm{R(E_n)} = \frac{\sigma_{\mathrm{A_1(n,f)}}(\mathrm{E_n})}{\sigma_{\mathrm{A_2(n,f)}}(\mathrm{E_n})} \tag{1}$$

of the cross sections of two compound-nuclear reactions, $\mathrm{n+A_1} \rightarrow \mathrm{B_1^*} \rightarrow \mathrm{f}$ and $\mathrm{n+A_2} \rightarrow \mathrm{B_2^*} \rightarrow \mathrm{f}$, is determined in two surrogate experiments. With an independent determination of one cross section, the ratio can then be used to deduce the other cross section.

The more general surrogate method involves analysis of the direct-reaction entrance channel, and requires a precise determination of the exit channel efficiencies. Analyzing the direct-reaction entrance channel is often difficult, as reactions on contaminants are indistinguishable from the reaction under consideration. The surrogate ratio method avoids this problem by using the ratio in

* casperson1@llnl.gov

Eq. 1, in which the detector efficiencies and challenges related to the direct-reaction entrance channels cancel out, leaving much cleaner data for the coincidence events that include both the direct-reaction ejectile and observables related to the exit channels.

In the Weisskopf-Ewing limit, the ratio in Eq. 1 takes the form:

$$\mathrm{R(E_n)} = \frac{\sigma_{\mathrm{n}}^{\mathrm{CN1}}(\mathrm{E_n})\ \mathcal{G}_{\mathrm{f}}^{\mathrm{CN1}}(\mathrm{E_n})}{\sigma_{\mathrm{n}}^{\mathrm{CN2}}(\mathrm{E_n})\ \mathcal{G}_{\mathrm{f}}^{\mathrm{CN2}}(\mathrm{E_n})}\ . \tag{2}$$

where $\sigma_{\mathrm{n}}^{\mathrm{CN1}}$ and $\sigma_{\mathrm{n}}^{\mathrm{CN2}}$ refer to the compound-nucleus formation cross sections for the reactions $\mathrm{n+A_1} \rightarrow \mathrm{B_1^*}$ and $\mathrm{n+A_2} \rightarrow \mathrm{B_2^*}$, and $\mathcal{G}_{\mathrm{f}}^{\mathrm{CN1}}$ and $\mathcal{G}_{\mathrm{f}}^{\mathrm{CN2}}$ denote the probabilities that the compound nuclei decay by fission. For most cases of interest, the compound-nucleus formation cross sections $\sigma_{\mathrm{n}}^{\mathrm{CN1}}$ and $\sigma_{\mathrm{n}}^{\mathrm{CN2}}$ can be calculated reliably by using an optical model. To determine $\mathcal{G}_{\mathrm{f}}^{\mathrm{CN1}}(\mathrm{E_n})$ / $\mathcal{G}_{\mathrm{f}}^{\mathrm{CN2}}(\mathrm{E_n})$, two experiments are carried out that create the relevant compound nuclei, CN1 and CN2. For each experiment, the number of coincidence events, $\mathrm{N}_{(\mathrm{p,tf})}^{\mathrm{CN1}}$ and $\mathrm{N}_{(\mathrm{p,tf})}^{\mathrm{CN2}}$, is measured. After accounting for differences in the target thickness, integrated beam charge, and live times of the two experiments, the ratio of the coincidence events can be set equal to the ratio $\mathcal{G}_{\mathrm{f}}^{\mathrm{CN1}}/\mathcal{G}_{\mathrm{f}}^{\mathrm{CN2}}$.

The reaction of interest for this work is ^{240}Am(n,f), which has never been measured above 4 MeV neutron energy. The isotope ^{240}Am has a half-life of 2.1 days, and the rapid decay of this nucleus makes it difficult to use as a target. The same compound system, ^{241}Am*, can be populated through the reaction ^{243}Am(p,t)^{241}Am*, and the 7370 year half-life of ^{243}Am makes it a much more reasonable choice as a target. For the other half of the ratio, the ^{238}U(p,t) reaction was used as a surrogate for the ^{235}U(n,f) reference reaction. Using the surrogate ratio method in this case, the formula for the cross section of ^{240}Am(n,f) reduces to

$$\sigma(^{240}\mathrm{Am(n,f)},\mathrm{E_n}) = \frac{\mathrm{N}^{\mathrm{CN1}}(^{243}\mathrm{Am(p,tf)},\mathrm{E_n})}{\mathrm{N}^{\mathrm{CN2}}(^{238}\mathrm{U(p,tf)},\mathrm{E_n})} \times \frac{\sigma_{\mathrm{n}+^{240}\mathrm{Am}}^{\mathrm{CN1}}(\mathrm{E_n})}{\sigma_{\mathrm{n}+^{235}\mathrm{U}}^{\mathrm{CN2}}(\mathrm{E_n})}\sigma(^{235}\mathrm{U(n,f)},\mathrm{E_n}) \tag{3}$$

where $\mathrm{E_n}$ refers to equivalent neutron energy. The reference reaction ^{235}U(n,f) is well known, and the values for the cross section are adapted from the ENDF/B-VII standard [19]. The ratio of N(^{243}Am(p,tf),E) to N(^{238}U(p,tf),E) that appears in Eq. 3 refers to the number of (p,tf) events that were measured on the two targets during this work, and these values must be scaled appropriately using the target thicknesses, integrated beam charge, and the live time correction factor. The ratio of $\sigma_{\mathrm{n}+^{240}\mathrm{Am}}^{\mathrm{CN1}}(\mathrm{E})$ to $\sigma_{\mathrm{n}+^{235}\mathrm{U}}^{\mathrm{CN2}}(\mathrm{E})$ refers to the compound nucleus formation cross section for neutrons interacting with the desired target nucleus ^{240}Am, and the reference nucleus ^{235}U. These values are calculated theoretically.

The following sections of this paper describe the measurement of ^{243}Am(p,tf) and ^{238}U(p,tf), and the determination of the ^{240}Am(n,f) cross section. Section II describes the STARLiTeR array, and the experimental procedure for performing these measurements. Section III gives a prescription for the analysis of STARLiTeR data, and gives results from the ^{243}Am(p,tf) and ^{238}U(p,tf) measurements. Section IV describes how the measured values are combined to produce the ^{240}Am(n,f) cross section.

II. EXPERIMENTAL PROCEDURE

The experiment was fielded using the newly installed and upgraded **S**ilicon **T**elescope **A**rray for **R**eactions with **Li**vermore, **Te**xas A&M University, and University of **R**ichmond, STARLiTeR. The physical detector arrangement of STARLiTeR is identical to the STARS-LIBERACE detector arrangement that was previously located at the 88" Cyclotron [20] at Lawrence Berkeley National Laboratory, and includes a silicon telescope, as well as an array of high-purity germanium segmented clover detectors with BGO Compton suppression shielding. The most significant difference between the two incarnations of the detector system is the completely new VME-based data acquisition system. The STARLiTeR array is positioned on a K150 beamline in the Cyclotron Institute at Texas A&M University, and for these measurements, a 1.5 nA 38.4 MeV proton beam was used to produce (p,p'), (p,d) and (p,t) reactions on a 52(3) μg/cm^2 ^{243}Am target and a 236(14) μg/cm^2 ^{238}U target. Each actinide target was created by electroplating enriched isotopes onto a 100 μg/cm^2 natural carbon backing [21], and the short half-life of the ^{243}Am target was the limiting factor for the target thickness, due to α-backgrounds in the fission detector.

The STARLiTeR silicon telescope was made from three S2 Micron detectors with thicknesses of 150 μm, 1005 μm, and 1000 μm. These detectors were labeled ΔE, E1, and E2 respectively, and a diagram of the silicon telescope can be seen in Fig. 1. The adjacent rings and sectors of the silicon detectors were bussed together by a circuit board to form effectively 24 rings and 8 sectors on each detector. The inner radius of these annular detectors is 11 mm, and each of the 24 rings has a width of 1 mm. The ring side of each silicon detector included a 0.1 μm aluminum contact, and the sector side included a 0.26 μm gold contact. The silicon telescope was located 18 mm downstream of the target, covering an angle range from 30 to 62 degrees. Between the target and the telescope was a 16 μm aluminum shield, to protect the 150 μm detector from δ-electrons, fission fragments, and α-decays from the ^{243}Am target. Located 14 mm upstream of the target, a 149 μm thick Micron S2 detector was used to detect fission events, and due to the similar stopping range of the fission fragments and α-particles in this experiment, protecting the detector with an aluminum shield was not possible. The raw α rate in the fission detector from the ^{243}Am target was about 27 kHz.

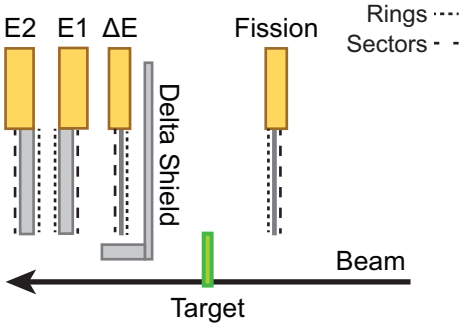

FIG. 1. (Color online) Cross section view of the silicon telescope (not to scale). The detector arrangement is cylindrical with respect to the beam axis. The gray regions represent the physical dimension of the silicon layer. The dashing on each side of the silicon represents the geometric subdivision of the contacts.

Surrounding the silicon telescope were six high-purity germanium segmented clover detectors, each with BGO Compton suppression shielding. The data collected with these detectors was not used during the determination of the ^{240}Am(n,f) cross section.

The excitation energy of the product nucleus is determined from the measured particle energy and the nuclear recoil. A full reconstruction of the recoiling nucleus energy can be determined using the energy of the beam, the scattered particle type (e.g. p, d, or t), and the angle with respect to the incoming beam. A table of the relevant Q-values and neutron separation energies, S_n, can be seen in Table I. The relationship between the particle energies for the ^{243}Am(p,tf) reaction and the ^{240}Am(n,f) reaction can be seen in Fig. 2. The triton Coulomb barrier occurs at around 12 MeV triton energy for Z=95, which can be seen to correspond to an equivalent neutron energy of 16 MeV. To avoid systematic effects due to the differences in the Coulomb barriers for a given equivalent neutron energy on ^{240}Am and ^{235}U, only neutron energies below 14 MeV were used to determine the ^{240}Am(n,f) cross section.

The experiment took place over a 9 day period and ran at rates of up to 12 kHz of data being written to disk. The recently commissioned VME-based data acquisition system used to record the events required a fixed non-updating deadtime of 25 μs per event, and produced an average live time fraction of 75%. The VME electronics used to take data consisted of five Mesytec MADC-32 modules, one Struck SIS3820 scaler module, and one CAEN V1190A TDC module. The MADC-32 modules are 13-bit, 32-channel ADCs that record the pulse-height and the clock-cycle that the trigger arrived in. The V1190A 128-channel TDC has 100 ps timing resolution, and records both the time relative to the trigger, and the clock cycle the trigger arrived in. This information was used to construct a 100 ps time stamp for each channel relative to the start of the run. The SIS3820 32-channel scaler was set to record the number of signals

TABLE I. The neutron separation energies of the compound nucleus, and the Q-values of the (p,t) reactions are shown for the two targets. The relevant nuclei have the following ground-state spins and parities:^{243}Am has $J^\pi = 5/2^-$, ^{238}U has $J^\pi = 0^+$, ^{240}Am has $J^\pi = (3^-)$, and ^{235}U has $J^\pi = 7/2^-$.

Reaction	CN	S_n (MeV)	Surrogate	Q-value (MeV)
^{240}Am(n,f)	^{241}Am	6.647	^{243}Am(p,tf)	-3.421
^{235}U(n,f)	^{236}U	6.545	^{238}U(p,tf)	-2.798

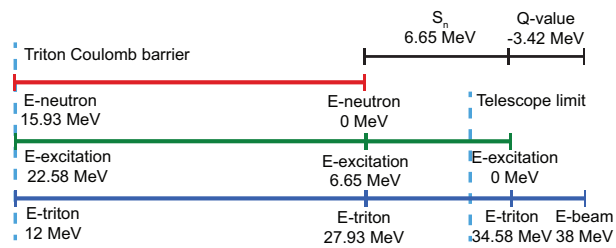

FIG. 2. (Color online) A diagram illustrating how the triton particle energy in the reaction ^{243}Am(p,tf) relates to the neutron energy in the reaction ^{240}Am(n,f). The bottom bar represents charged particle energies, the middle bar represents nuclear excitation energy, and the top bar represents equivalent neutron energy. S_n is the neutron separation energy of ^{241}Am, and Q-value refers to the Q-value of the ^{243}Am(p,t) reaction. The telescope limit dashed line represents the maximum triton energy that the telescope can stop for the angle ranges of interest.

of various types that arrive in each one-second interval. The ADC and TDC modules were time-stamped with a common 40 MHz clock, generated from an Agilent Technologies 33250A Function Generator with a frequency accuracy of 2 ppm. The function and purpose of the various components will be described in the following sections.

III. ANALYSIS

A. Gating

A number of multidimensional gates were used throughout the analysis to generate one-dimensional and two-dimensional projections of the data, and a list of gates used in the analysis is given in Table II. Due to a limited number of channels in the VME discriminators, timing information for the E2 silicon detector was not recorded. This would have been a valuable gate for removing beam that scatters off of the aluminum δ-shield tunnel, and without that gate available, the RT2 gate plays a significant role in removing these events.

TABLE II. The physical meaning of the various gates utilized in the analysis of this measurement.

Name	Meaning
PID	Particle identification using ΔE-E energies
RT1	Ray-trace condition using ΔE-E1 detectors
RT2	Ray-trace condition using E1-E2 detectors
PFT	Particle-fission time difference

B. Event reconstruction

A valid event was triggered when the energy deposited into both the ΔE and E1 detectors exceeded the minimum threshold of the VME leading edge discriminators. The discriminator thresholds were set as low as possible above the electronic noise, and the typical energy threshold for this measurement was 300 keV for the ΔE, and 500 keV for the E1 and E2 detectors. A scaler module recorded the raw ΔE, E1, E2, fission, and clover detector rates, as well as the raw trigger rate and the deadtime-vetoed trigger rate. General (p,tf) statistics were monitored throughout the measurement using an online analyzer, to ensure an appropriate balance of statistics for the ^{243}Am and ^{238}U targets.

The ring with the highest energy for each event was identified for the ΔE and E1 detectors, in order to ray-trace the events that originated from the target, and to exclude events that occurred upstream from the beam collimator. Using the position along the beam axis of each detector plane, and the radius of the rings that fired, the intersection of the particle ray with the target plane could be calculated. Using this technique, the time-averaged beam spot was observed to have a diameter of less than 6 mm. Various backgrounds could be removed by only including events that originate from the beam spot. The ray-trace condition corresponding to ΔE and E1 is referred to as RT1, as listed in Table II. A similar ray trace condition was applied between the E1 and E2 detectors, and this condition is referred to as RT2.

Valid events were also checked to ensure that the sectors were aligned, indicating that the particle produced a straight path coming from the target to its final stopping place in one of the detectors. This was a strict requirement during the event reconstruction, which was enforced prior to any gating. The full energy of the event was reconstructed by adding the energy of the sectors together from the ΔE, E1, and E2 detectors, if the particle penetrated that far into the detector telescope. Once the full energy of the scattered particle was known, the Q-value of the reaction was subtracted from the measured energy, and a correction for the kinematic recoil of the nucleus was applied. From this final energy, the precise excitation energies of the ^{236}U and ^{241}Am nuclei could be determined.

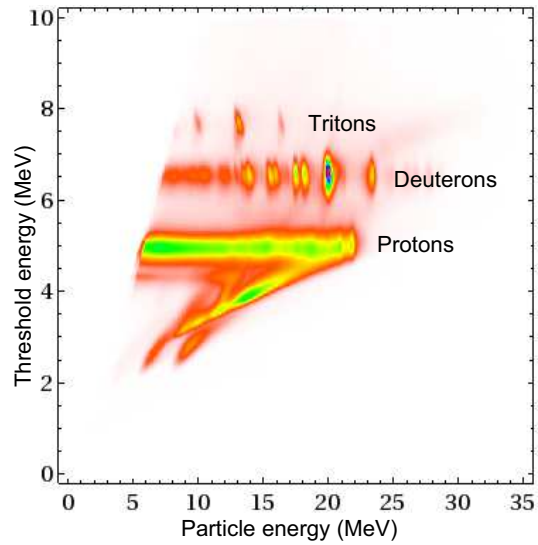

FIG. 3. (Color online) The raw spectrum of outgoing particles p, d, and t, identified using the silicon telescope. Plotted are the results of the range-energy relation for all hydrogen isotopes that were identified as passing through a specific ring of the ΔE detector from the ^{243}Am target. The y-axis represents the threshold energy for the given particle type passing through the ΔE detector. The three discrete states seen in the tritons, which have the largest range-energy value shown, originate from (p,t) reactions on carbon and oxygen contaminants in the target.

TABLE III. Sources of energy uncertainty. Listed as average values over 30 to 62 degree angle range for tritons.

Description	Energy uncertainty (keV)
^{238}U target	3
Kinematic uncertainty	5
Aluminum δ-shield	10
Gold surface layer	12
ΔE detector	30
E1 detector	37
E2 detector	48
Total energy uncertainty	70

C. Calibration

The silicon detector energies were calibrated at the beginning and end of the experiment using a standard Eckert-Ziegler Type A-2 nominal 100 nCi ^{226}Ra α source. The spot size of the electroplated ^{226}Ra is 5 mm in diameter. The α-decays from ^{226}Ra and its daughters have energies of 4.784, 5.489, 6.002, 7.687 MeV, and these were used to calibrate the ΔE, E1, and E2 detectors. Unlike the α-particles produced by the ^{226}Ra source, the protons, deuterons, and tritons that the silicon telescope detects pass through a 16 μm aluminum shield, as well as a number of aluminum and gold contacts on the ΔE, E1, and E2 detectors. The energy lost in these inac-

tive layers was calculated using the code ELAST [22], and the measured particle energies were corrected using this information. During the experiment, (p,t) reactions on carbon and oxygen contaminants were observed, and these were used to perform an in-beam secondary calibration. This correction was performed for each sector, and the distribution of sector corrections had a standard deviation of approximately 25 keV.

The expected energy uncertainty includes contributions from the intrinsic uncertainty of the detectors, energy straggling through the target, δ-shield, and gold layer on the detectors, and angular uncertainty, which affects the recoil correction. Adding these contributions together in quadrature yields a 70 keV 1-σ energy uncertainty. The contributions to the energy resolution are summarized in Table III. Verifying this uncertainty experimentally is difficult, as the ^{12}C(p,t)^{10}C and ^{16}O(p,t)^{14}O reactions that produce discrete lines in particle spectra have a much larger energy uncertainty, due to the large kinematic correction, and the angular uncertainty inherent in the particle detection. The intrinsic detector resolution scaled approximately as $\sqrt{\mathrm{E}}$, which resulted in a larger uncertainty for high-energy tritons from the (p,t) reaction than for the alphas from the ^{226}Ra source. This scaling was assumed in Table III.

The target thicknesses were determined by α-counting the targets using an additional 150 μm thick silicon detector, which had been previously calibrated using the ^{226}Ra α source. An 8.34 mm diameter aluminum mask was placed in front of each target, to represent the portion of the target exposed to beam. The α-rate from the ^{238}U target was extremely low, and background α-lines from radon daughters had to be accounted for during the analysis. Due to scattering in the target, uncertainties in the masking, and gating restrictions caused by contaminants, a systematic uncertainty of 6% would be assigned to each target for absolute activity. Fortunately, many of these uncertainties cancel out when taking a ratio of the two target thicknesses, and the uncertainty of the ratio was found to be 3%.

D. Particle identification

All of the events in which energy was deposited in both the ΔE and E1 detectors were analyzed, and the triton band was identified using the following range-energy equation:

$$R = (E_{\mathrm{total}}^{1.68} - E_{\mathrm{E1+E2}}^{1.68})^{1/1.68}, \tag{4}$$

A particle identification plot that was generated with this function can be seen in Fig. 3. This function generates a value which is closely related to the minimum energy that will allow a given particle type to pass through the 150 μm ΔE detector. The exact value of the exponent is related to the stopping power of silicon, and can depend on the inactive regions of the telescope, both during the calibration and during the experiment. Here, $\mathrm{E_{total}}$ is the total energy of the particle detected, and $\mathrm{E_{E1+E2}}$ is the total energy deposited in the E1 and E2 detectors of the silicon telescope.

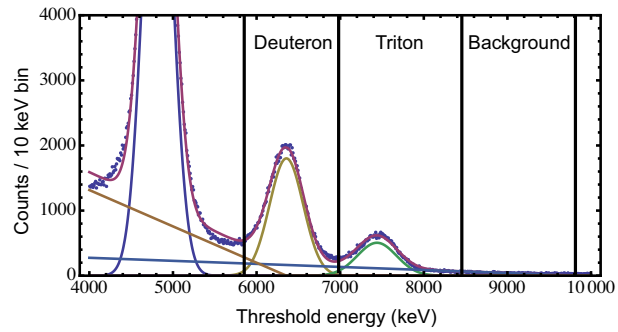

FIG. 4. (Color online) Projected range-energy spectrum for a specific ring in the ^{243}Am(p,tf) data set, illustrating the fitting procedure. Events in each region, and theoretical contributions of each particle type were separated by solving a linear equation, in order to extract the triton spectrum.

One possible source of error in particle identification analysis is cross-contamination of deuterons into the triton spectrum of the range-energy projection. Fig. 4 illustrates the particle contributions in the various regions of the range-energy projection, specifically highlighting deuteron dominant, triton dominant, and background dominant regions. The random background has a broad linear distribution, the triton spectrum has a gaussian shape, and the deuteron spectrum consists of both a gaussian distribution, and a linear tail on the low-energy side, corresponding to deuterons punching through the telescope.

To extract the triton spectrum, a matrix of the integrated contributions of the three distributions in the three regions was calculated. The matrix was then inverted, yielding the triton distribution as a function of the three regions. By taking a projection of the data in the three regions, and multiplying these projections by the weights in the inverted matrix, the pure particle spectrum could be generated. The particle identification gate that these weights represent is referred to as PID, as listed in Table II.

One of the assumptions used when placing gates like this is that the multidimensional distribution of the various features is a product of independent distributions in each dimension. The linear tail on the low-energy side of the deuteron peak does not satisfy this condition, as it is a diagonal distribution in the dimensions of total energy and the range-energy value. To reduce the systematic error from this inaccurate assumption, the deuteron punch-through was not considered to be part of the theoretical deuteron shape.

The fission events were detected using a 149 μm thick silicon Micron S2 detector located upstream of the target. The total fission spectrum for all detected events can be seen in Fig. 5. The raw spectrum shown in that figure is scaled down by a factor of 45, in order to compare it to

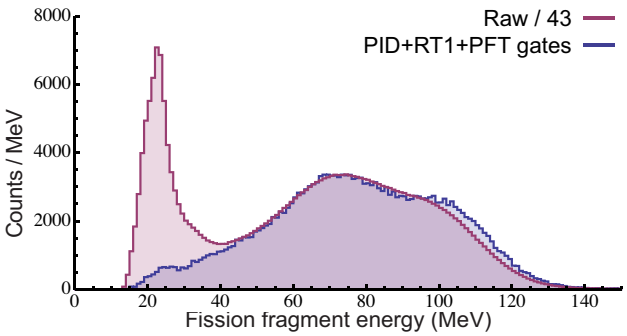

FIG. 5. (Color online) The gated fission spectrum for ^{243}Am(p,tf) events from all rings for the entire ^{243}Am data set, compared to the raw fission spectrum for the ^{243}Am target without gates. The raw fission spectrum has been scaled down by a factor of 43, for comparison. The large low-energy peak in raw spectrum is suspected to result from ^{12}C(p,p'α) in the ^{nat}C backing.

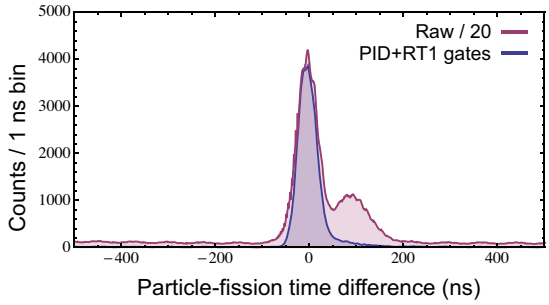

FIG. 6. (Color online) The particle-fission timing spectrum shows a gated spectrum with a prompt region where tritons and fission fragments from the same event are detected. Also shown in the plot is the raw ungated data, scaled down by a factor of 20, for comparison. The peak at later times in the raw spectrum is suspected to result from ^{12}C(p,p'α) in the ^{nat}C backing.

the spectrum including PID+RT1+PFT gates. The large feature that appears at low fission energies is beam scattered by the collimator, depositing energy in the fission detector and the silicon telescope. The PID gate plays the most significant role in removing this background, as it is most likely that the scattered particle detected in the silicon telescope is a proton.

The particle-fission relative timing shown in Fig. 6 was measured by subtracting the TDC value of the particle from the TDC value of fission fragment, and this allowed for identification of the prompt and random fission events. The raw data shown in that figure is scaled down by a factor of 20, in order to compare it to the spectrum including PID+RT1 gates. The gate corresponding to the removal of background events from the prompt region in the particle-fission timing spectrum is referred to as PFT, as listed in Table II. The peak at later times in the raw spectrum of Fig. 6 is attributed to α particles from the ^{12}C(p,p'α) in the ^{nat}C backing of both targets.

The structure of the particle-fission timing spectrum

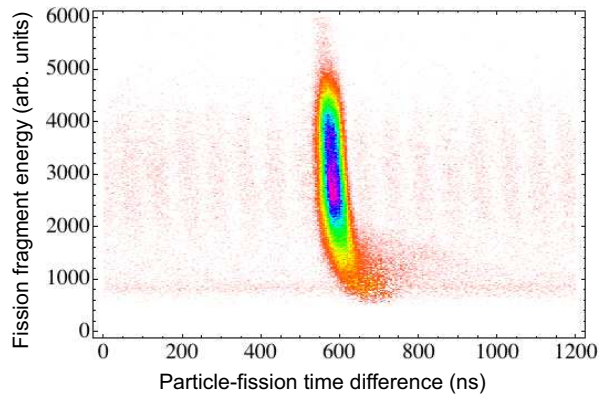

FIG. 7. (Color online) The fission energy versus particle-fission timing. The smearing near the lower energy edge of the fission fragment distribution represents remnants of scattered beam, which has been gated out using the PID and RT1 gates.

can be clarified by plotting the fission-fragment energy against the particle-fission timing, as in Fig. 7. The smearing that is visible on the low fission energy portion of this figure is suspected to result from ^{12}C(p,tα) in the ^{nat}C backing, which has a lower rate than the ^{12}C(p,p'α) peak that is visible in the raw data of Figs. 5 and 6. An additional cut was placed on the fission energy above the peak structure, in order reduce the systematic error from this contaminant.

The final step in the analysis was to calculate the excitation energy of the compound ^{241}Am and ^{236}U nuclei, using the kinematically corrected triton energies, and then to convert the excitation energies into equivalent neutron energies for the desired ^{240}Am and ^{235}U target nuclei. An illustration of this energy arithmetic was shown in Fig. 2.

There are then four detector scenarios that need to be considered when generating the spectra of ^{243}Am(p,tf) and ^{238}U(p,tf) events. The simplest scenario is that only detectors ΔE and E1 fired in a given event, and the particle energy in this case is calculated with ΔE+E1. The appropriate gates for this situation are PID+RT1+PFT. The next scenario to be considered occurs when ΔE, E1, and E2 all fired in a given event, and the particle energy in this case is calculated with ΔE+E1+E2. In this case the appropriate gates are PID+RT1+RT2+PFT.

There is a more complicated third scenario that can occur in this measurement where a random coincidence of scattered beam in E2 would otherwise cause a rejection of a real event in ΔE+E1. The total energy in this case is ΔE+E1, and the appropriate gates are PID+RT1$-$RT2+PFT, where $-$RT2 refers to events that fail the RT2 ray-trace condition. A time difference gate between ΔE and E2 would have been much more effective at removing these events than RT2, but the limited number of channels in the 128-channel TDC resulted in a lack of timing information for the E2 detector.

To generate the final spectra for ^{243}Am(p,tf) and ^{238}U(p,tf), gated events from all three scenarios must be

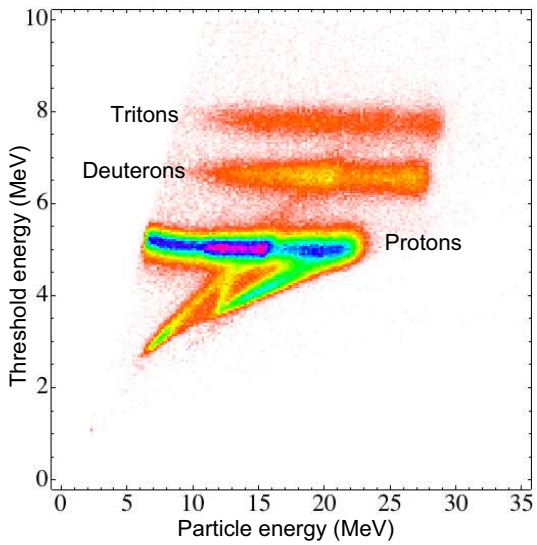

FIG. 8. (Color online) PFT+RT1+RT2 gated spectrum of outgoing particles p, d, and t, identified using the silicon telescope. Plotted are the results of the range-energy relation for all hydrogen isotopes that were identified as passing through a specific ring of the ΔE detector from the ^{243}Am target. The y-axis represents the threshold energy for the given particle type passing through the ΔE detector. No carbon or oxygen contamination is visible, due to the PFT gate. The RT1+RT2 gates reduce the amount of scattered beam visible in the plot.

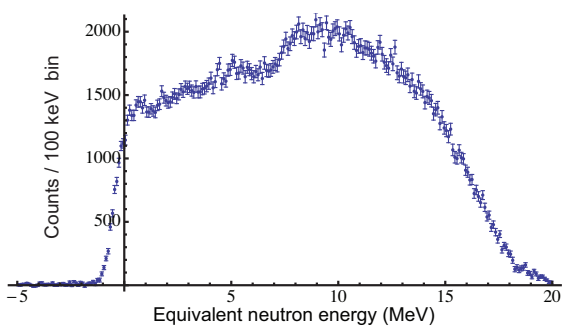

FIG. 9. (Color online) The spectrum of ^{243}Am(p,tf) events, plotted as a function of equivalent neutron energy.

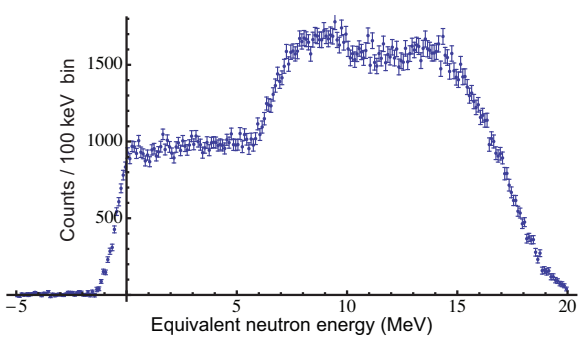

FIG. 10. (Color online) The spectrum of ^{238}U(p,tf) events, plotted as a function of equivalent neutron energy.

TABLE IV. The experimental error budget for the systematic uncertainty in the ^{240}Am(n,f) cross section.

Description	Uncertainty
Target thickness ratio	3%
Target thickness variation	4%
Ratio of integrated beam current	≤1%
Ratio of live time fraction	≤1%
Uncertainty in ^{235}U cross section	1%
Total systematic uncertainty	5%

added together. Leaving out the PID gate allows for the creation of a gated particle identification plot, illustrating the removal of many contaminants in the hydrogen isotope data. An example of such a gated plot can be seen in Fig. 8, and should be compared to the raw data in Fig. 3. The PID-gated ^{243}Am(p,tf) and ^{238}U(p,tf) data projected on the full energy axis can be seen in Figs. 9 and 10 respectively.

E. Systematic uncertainties

The systematic uncertainties contributing to the overall uncertainty in the ^{240}Am(n,f) cross section include the target thickness ratio uncertainty, target thickness variation, uncertainty in the ratio of the beam current, uncertainty in the live time fractions, and the uncertainty in the ^{235}U(n,f) evaluation. A summary of these contributions is shown shown in Table IV. The integrated beam current and live time fractions were accurately measured throughout the measurement, and the uncertainties are assumed to be less than 1%. The uncertainty from the target thickness ratio was described in Sec. III C.

The largest experimental systematic uncertainty in this measurement was from the variation of the target thickness over small distances. The (p,tf) event rate, when divided by total charge and live time fraction for a given run, was observed to vary by 4% over the course of the measurement. This variation was attributed to variations of the target thickness as the beam spot slowly wandered over these different regions of the target. Using the ray-trace analysis, the time-averaged beam spot was observed to be smaller than 6 mm in diameter, indicating that the region the beam drifted across was of a similar scale.

Combining all of these contributions together gives an overall experimental systematic uncertainty for this ratio measurement of 5%.

IV. DETERMINATION OF THE ^{240}Am(n, f) CROSS SECTION

The ^{240}Am(n,f) cross section can be determined from the ^{243}Am(p,tf) and ^{238}U(p,tf) measurements using the surrogate ratio method, by putting the relevant values

TABLE V. The scale factors needed to compare the ^{243}Am and ^{238}U data sets.

Reaction	Surrogate	Thickness (μg/cm^2)	Charge (μC)	Live (%)
^{240}Am(n,f)	^{243}Am(p,tf)	52	443.7	74.6
^{235}U(n,f)	^{238}U(p,tf)	236	86.3	74.2

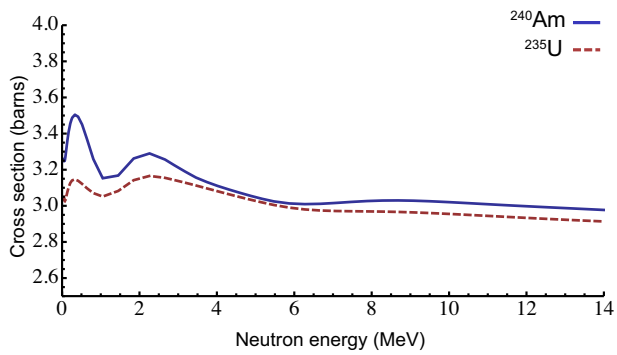

FIG. 11. (Color online) The calculated compound nucleus formation cross sections for ^{240}Am and ^{235}U.

into Eq. 3. The N(^{243}Am(p,tf),E) and N(^{238}U(p,tf),E) terms in the formula refer to the data shown in Figs. 9 and 10 respectively. This data includes the kinematic recoil energy correction and is defined in terms of equivalent neutron energy. In order to make the measurements on the two targets compatible, the data shown in those figures must be scaled by the target thickness, integrated beam charge, and live time fractions, which can be seen in Table V. The ^{235}U(n,f) cross section in Eq. 3 is the reference reaction term in the ratio formula, and the data for this was adapted from the ENDF/B-VII standard [19].

An essential ingredient in the ratio formula, Eq. 2, is the ratio of the compound nucleus formation cross sections for n+^{240}Am and n+^{235}U. These cross sections can be determined from an appropriate coupled-channels calculation that takes into account a sufficient number of rotational states in the deformed target nuclei [23]. We employed the code ECIS06 [24] and used the optical-model potential developed by Soukhovitskii *et al.* [25]. Rotational bands with 9 states for ^{240}Am, and 8 states for ^{235}U, were found to produce well-converged total and compound-formation cross sections. Applying the same procedure to the nearby ^{241}Am and ^{238}U isotopes produces total cross sections that are in good agreement with available experimental results. The uncertainty in the compound-formation cross sections is estimated to be about 5% above 2 MeV neutron energy and 10% for smaller neutron energies. An uncertainty of 3% above 2 MeV neutron energy is found for the ratio of the compound-formation cross sections by accounting for correlations in the two cross sections. The calculated cross sections can be seen in Fig. 11.

Inserting all of these components into Eq. 3 yields the ^{240}Am(n,f) cross section as a function of neutron energy. As shown in Fig. 2, the triton Coulomb barrier becomes significant at 16 MeV equivalent neutron energy. The effect of the Coulomb barrier gradually becomes more significant over the range of a few MeV, and can influence the cross section even down to 14 MeV equivalent neutron energy. A given equivalent neutron energy corresponds to triton energies that differ by about 500 keV for the two targets, and the different Coulomb barrier effects at these two energies can create a systematic error in the ratio. In order to minimize these effects, the equivalent neutron energy in the final result has been cut off at 14 MeV.

The cross section of ^{240}Am(n,f) with error bars can be seen in Fig. 12, in comparison with the existing surrogate measurements up to 4 MeV equivalent neutron energy. The data represented by the red squares [26] used the surrogate method by multiplying the fission probabilities for the excited ^{241}Am nucleus by the formation cross section. The fission probabilities were determined by measuring the ^{240}Pu(^{3}He,df) reaction [27]. This data was reanalyzed with modern surrogate methods to produce the data represented by the green triangles in Fig. 12 [28]. The uncertainties for the green triangle data was determined to be 10%, which is compatible with the results found in this work, above 2 MeV. Below 2 MeV neutron energy, the Weisskopf-Ewing approximation is known to be less valid, which accounts for the differences in the resulting cross sections for the ^{240}Pu(^{3}He,df) and ^{243}Am(p,tf) surrogate reactions.

The cross section of ^{240}Am(n,f) with error bars can be seen in Fig. 13, in comparison with the existing estimates in ENDL2009 [29], JENDL-4.0 [30], ENDF/B-VII.1 [31], ENDL2011, ROSFOND-2010 [32], and CENDL-3.1 [33]. The ENDF/B-VII.1 and ENDL2011 cross sections adopted the values from JENDL-4.0, and all three are represented by the same line in Fig. 13. The ENDL2009 evaluation most closely matches the cross section determined in this work above 2 MeV neutron energy. A possible reason for this is that the ENDL2009 evaluation included the surrogate data [28] for neutron energies below 4 MeV, and likely used the values near 4 MeV to constrain the model that was used to extend the evaluation to higher energies. As ENDL2011 adopted the values from JENDL-4.0, the most recent evaluations no longer resemble the cross section that was found in this work, and a reevaluation of the ^{240}Am(n,f) cross section is recommended.

The ^{240}Am(n,f) cross section has been measured down to 50 keV equivalent neutron energy, but with the estimated 70 keV energy resolution, contributions from negative neutron energies cannot be excluded from sufficiently low equivalent neutron energies. The behavior of the ^{243}Am(p,tf) and ^{238}U(p,tf) data at negative neutron energies can be seen in Figs. 9 and 10. To compensate for this issue, only data above 200 keV equivalent neutron energy are recommended.

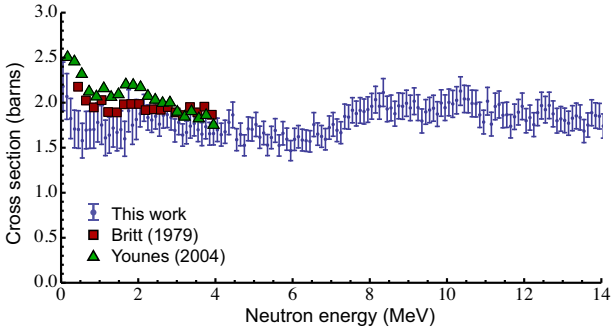

FIG. 12. (Color online) The ^{240}Am(n,f) cross section from this work compared to the existing existing data measured using the surrogate method up to 4 MeV equivalent neutron energy [26, 28].

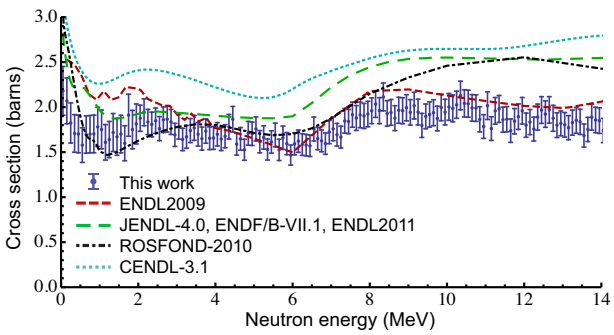

FIG. 13. (Color online) The ^{240}Am(n,f) cross section from this work compared to the existing estimates in ENDL2009, JENDL-4.0, ENDF/B-VII.1, ENDL2011, ROSFOND-2010, and CENDL-3.1.

V. CONCLUSIONS

We have measured the ^{240}Am(n,f) cross section using the surrogate ratio method over an energy range of 200 keV to 14 MeV. The isotope ^{240}Am is produced in nuclear reactors, and an incorrect cross section for neutron-induced fission could influence estimates of long-lived actinide waste. This cross section has never been directly measured, due to the short half-life of the ^{240}Am nucleus, and had only been previously measured with the surrogate method up to 4 MeV. The isotope ^{243}Am has a much longer half-life than ^{240}Am, which made it a more practical target for producing the ^{241}Am compound nucleus. The ^{243}Am(p,tf) and ^{238}U(p,tf) nuclear reactions were measured as surrogates for ^{240}Am(n,f) and ^{235}U(n,f) respectively, using the STARLiTeR detector system on the K150 beam line at the Texas A&M University Cyclotron Institute. The ^{240}Am(n,f) cross section obtained in this work disagrees with the ENDL2011, ENDF/B-VII.1, JENDL-4.0, ROSFOND-2010, and CENDL-3.1 evaluations, and we recommend that the ^{240}Am(n,f) cross section be reevaluated taking into account the results of this work.

ACKNOWLEDGMENTS

We wish to acknowledge the efforts of the Texas A&M Cyclotron Institute's staff for their outstanding efforts on this first STARLiTeR experiment. In particular we thank George Kim, Fred Abegglen, Erik Yendrey, Henry Clark and Leigh Gathings. We would also like to thank Frank S. Dietrich (LLNL) for useful discussions. This work performed under the auspices of the U.S. Department of Energy by Lawrence Livermore National Laboratory under Contract DE-AC52-07NA27344, the Department of Energy's NNSA Office of Defense Nuclear Nonproliferation Research & Development, and the Texas A&M Cyclotron Institute under grants DE-FG52-09NA29467 from NNSA and DE-FG02-93ER40773 from the DOE Office of Nuclear Physics.

[1] J. D. Cramer and H. C. Britt, Nucl. Sci. Eng. **41**, 177 (1970).
[2] J. D. Cramer and H. C. Britt, Phys. Rev. C **2**, 2350 (1970).
[3] M. Petit, M. Aiche, G. Barreau, S. Boyer, N. Carjan, S. Czajkowski, D. Dassi, C. Grosjean, A. Guiral, B. Haas, D. Karamanis, S. Misicu, C. Rizea, F. Saintamon, S. Andriamonje, E. Bouchez, F. Gunsing, A. Hurstel, Y. Lecoz, R. Lucas, C. Theisen, A. Billebaud, L. Perrot, and E. Bauge, Nuclear Physics A **735**, 345 (2004).
[4] C. Plettner, H. Ai, C. W. Beausang, L. A. Bernstein, L. Ahle, H. Amro, M. Babilon, J. T. Burke, J. A. Caggiano, R. F. Casten, J. A. Church, J. R. Cooper, B. Crider, G. Gürdal, A. Heinz, E. A. McCutchan, K. Moody, J. A. Punyon, J. Qian, J. J. Ressler, A. Schiller, E. Williams, and W. Younes, Phys. Rev. C **71**, 051602 (2005).
[5] J. T. Burke, L. A. Bernstein, J. Escher, L. Ahle, J. A. Church, F. S. Dietrich, K. J. Moody, E. B. Norman, L. Phair, P. Fallon, R. M. Clark, M. A. Deleplanque, M. Descovich, M. Cromaz, I. Y. Lee, A. O. Macchiavelli, M. A. McMahan, L. G. Moretto, E. Rodriguez-Vieitez, F. S. Stephens, H. Ai, C. Plettner, C. Beausang, and B. Crider, Phys. Rev. C **73**, 054604 (2006).
[6] B. F. Lyles, L. A. Bernstein, J. T. Burke, F. S. Dietrich, J. Escher, I. Thompson, D. L. Bleuel, R. M. Clark, P. Fallon, J. Gibelin, A. O. Macchiavelli, M. A. McMahan, L. Phair, E. Rodriguez-Vieitez, M. Wiedeking, C. W. Beausang, S. R. Lesher, B. Darakchieva, and M. Evtimova, Phys. Rev. C **76**, 014606 (2007).
[7] B. K. Nayak, A. Saxena, D. C. Biswas, E. T. Mirgule, B. V. John, S. Santra, R. P. Vind, R. K. Choudhury, and S. Ganesan, Phys. Rev. C **78**, 061602 (2008).
[8] S. R. Lesher, J. T. Burke, L. A. Bernstein, H. Ai, C. W. Beausang, D. L. Bleuel, R. M. Clark, F. S. Dietrich, J. E.

Escher, P. Fallon, J. Gibelin, B. L. Goldblum, I. Y. Lee, A. O. Macchiavelli, M. A. McMahan, K. J. Moody, E. B. Norman, L. Phair, E. Rodriguez-Vieitez, N. D. Scielzo, and M. Wiedeking, Phys. Rev. C **79**, 044609 (2009).

[9] M. Basunia, R. Clark, B. Goldblum, L. Bernstein, L. Phair, J. Burke, C. Beausang, D. Bleuel, B. Darakchieva, F. Dietrich, M. Evtimova, P. Fallon, J. Gibelin, R. Hatarik, C. Jewett, S. Lesher, M. McMahan, E. Rodriguez-Vieitez, and M. Wiedeking, Nuclear Instruments and Methods in Physics Research Section B: Beam Interactions with Materials and Atoms **267**, 1899 (2009).

[10] J. M. Allmond, L. A. Bernstein, C. W. Beausang, L. Phair, D. L. Bleuel, J. T. Burke, J. E. Escher, K. E. Evans, B. L. Goldblum, R. Hatarik, H. B. Jeppesen, S. R. Lesher, M. A. McMahan, J. O. Rasmussen, N. D. Scielzo, and M. Wiedeking, Phys. Rev. C **79**, 054610 (2009).

[11] B. L. Goldblum, S. R. Stroberg, J. M. Allmond, C. Angell, L. A. Bernstein, D. L. Bleuel, J. T. Burke, J. Gibelin, L. Phair, N. D. Scielzo, E. Swanberg, M. Wiedeking, and E. B. Norman, Phys. Rev. C **80**, 044610 (2009).

[12] G. Kessedjian, B. Jurado, M. Aiche, G. Barreau, A. Bidaud, S. Czajkowski, D. Dassi, B. Haas, L. Mathieu, L. Audouin, N. Capellan, L. Tassan-Got, J. Wilson, E. Berthoumieux, F. Gunsing, C. Theisen, O. Serot, E. Bauge, I. Ahmad, J. Greene, and R. Janssens, Physics Letters B **692**, 297 (2010).

[13] J. J. Ressler, J. T. Burke, J. E. Escher, C. T. Angell, M. S. Basunia, C. W. Beausang, L. A. Bernstein, D. L. Bleuel, R. J. Casperson, B. L. Goldblum, J. Gostic, R. Hatarik, R. Henderson, R. O. Hughes, J. Munson, L. W. Phair, T. J. Ross, N. D. Scielzo, E. Swanberg, I. J. Thompson, and M. Wiedeking, Phys. Rev. C **83**, 054610 (2011).

[14] R. O. Hughes, C. W. Beausang, T. J. Ross, J. T. Burke, N. D. Scielzo, M. S. Basunia, C. M. Campbell, R. J. Casperson, H. L. Crawford, J. E. Escher, J. Munson, L. W. Phair, and J. J. Ressler, Phys. Rev. C **85**, 024613 (2012).

[15] J. E. Escher, J. T. Burke, F. S. Dietrich, N. D. Scielzo, I. J. Thompson, and W. Younes, Rev. Mod. Phys. **84**, 353 (2012).

[16] A. Czeszumska, C. T. Angell, J. T. Burke, N. D. Scielzo, E. B. Norman, R. A. E. Austin, G. Boutoux, R. J. Casperson, P. Chodash, R. O. Hughes, C. M. Mattoon, V. Méot, J. Munson, L. Phair, J. J. Ressler, O. Roig, T. J. Ross, E. Swanberg, and B. Wang, Phys. Rev. C **87**, 034613 (2013).

[17] J. E. Escher and F. S. Dietrich, Phys. Rev. C **74**, 054601 (2006).

[18] J. E. Escher and F. S. Dietrich, Phys. Rev. C **81**, 024612 (2010).

[19] M. Chadwick, P. Obloinsk, M. Herman, N. Greene, R. McKnight, D. Smith, P. Young, R. MacFarlane, G. Hale, S. Frankle, A. Kahler, T. Kawano, R. Little, D. Madland, P. Moller, R. Mosteller, P. Page, P. Talou, H. Trellue, M. White, W. Wilson, R. Arcilla, C. Dunford, S. Mughabghab, B. Pritychenko, D. Rochman, A. Sonzogni, C. Lubitz, T. Trumbull, J. Weinman, D. Brown, D. Cullen, D. Heinrichs, D. McNabb, H. Derrien, M. Dunn, N. Larson, L. Leal, A. Carlson, R. Block, J. Briggs, E. Cheng, H. Huria, M. Zerkle, K. Kozier, A. Courcelle, V. Pronyaev, and S. van der Marck, Nuclear Data Sheets **107**, 2931 (2006).

[20] S. Lesher, L. Phair, L. Bernstein, D. Bleuel, J. Burke, J. Church, P. Fallon, J. Gibelin, N. Scielzo, and M. Wiedeking, Nuclear Instruments and Methods in Physics Research Section A: Accelerators, Spectrometers, Detectors and Associated Equipment **621**, 286 (2010).

[21] R. Henderson, J. Gostic, J. Burke, S. Fisher, and C. Wu, Nuclear Instruments and Methods in Physics Research Section A: Accelerators, Spectrometers, Detectors and Associated Equipment **655**, 66 (2011).

[22] Energy Loss and Straggle Tool [adapted from ENELOSS, written by H. Ernst (1981) and modified by K. Lesko (1984)].

[23] F. S. Dietrich, I. J. Thompson, and T. Kawano, Phys. Rev. C **85**, 044611 (2012).

[24] J. Raynal, Tech. Rep. CEA-N-2772, Commissariat a l'Energie Atomique, Paris, 1994.

[25] E. S. Soukhovitskii, S. Chiba, J.-Y. Lee, O. Iwamoto, and T. Fukahori, Journal of Physics G: Nuclear and Particle Physics **30**, 905 (2004).

[26] H. C. Britt and J. B. Wilhelmy, Nucl. Sci. Eng. **72**, 222 (1979).

[27] A. Gavron, H. C. Britt, E. Konecny, J. Weber, and J. B. Wilhelmy, Phys. Rev. C **13**, 2374 (1976).

[28] W. Younes, H. C. Britt, and J. A. Becker, UCRL-TR-201913, LLNL (2004).

[29] B. Beck *et al.*, LLNL-TR-452511, LLNL (2010).

[30] K. Shibata, O. Iwamoto, T. Nakagawa, N. Iwamoto, A. Ichihara, S. Kunieda, S. Chiba, K. Furutaka, N. Otuka, T. Ohasawa, T. Murata, H. Matsunobu, A. Zukeran, S. Kamada, and J.-I. Katakura, Journal of Nuclear Science and Technology **48**, 1 (2011).

[31] M. Chadwick, M. Herman, P. Obloinsk, M. Dunn, Y. Danon, A. Kahler, D. Smith, B. Pritychenko, G. Arbanas, R. Arcilla, R. Brewer, D. Brown, R. Capote, A. Carlson, Y. Cho, H. Derrien, K. Guber, G. Hale, S. Hoblit, S. Holloway, T. Johnson, T. Kawano, B. Kiedrowski, H. Kim, S. Kunieda, N. Larson, L. Leal, J. Lestone, R. Little, E. McCutchan, R. MacFarlane, M. MacInnes, C. Mattoon, R. McKnight, S. Mughabghab, G. Nobre, G. Palmiotti, A. Palumbo, M. Pigni, V. Pronyaev, R. Sayer, A. Sonzogni, N. Summers, P. Talou, I. Thompson, A. Trkov, R. Vogt, S. van der Marck, A. Wallner, M. White, D. Wiarda, and P. Young, Nuclear Data Sheets **112**, 2887 (2011).

[32] S.V. Zabrodskaya, A.V. Ignatyuk , V.N. Koscheev et al., ROSFOND - Rossiyskaya Natsionalnaya Biblioteka Nejtronnykh Dannykh, VANT, Nuclear Constants 1-2, 3 (2007).

[33] Z.G. Ge, Y.X. Zhuang, T.J. Liu, J.S. Zhang, H.C. Wu, Z.X. Zhao, H.H. Xia, Proc. International Conference on Nuclear Data for Science and Technology, Jeju Island, Korea, April 26-30, 2010 (in press).